Unraveling Molecular Assembly and Tracking Lipid Droplets Dynamics using Fluorescent Phenanthroimidazole Derivatives

Subhankar Kundu,[a] Bahadur Sk,[a] Nitu Saha,[b] Tapas Kumar Dutta,[a] Subhadeep Das,[a] Raghuvir Singh Tomar,*[b] Abhijit Patra*[a]

[a]Department of Chemistry, [b]Department of Biological Sciences, Indian Institute of Science Education and Research Bhopal, Bhopal By-Pass Road, Bhauri, Bhopal 462066, Madhya Pradesh, India

Email: rst@iiserb.ac.in, abhijit@iiserb.ac.in

ABSTRACT: A judicious structural modification of molecular building units imparts significant variation in the evolution dynamics of supramolecular self-assembled architectures and their functional properties. The incorporation of alkyl chains into the rigid and π-conjugated molecular backbone not only directs the self-assembly but also enhances the hydrophobicity of the probe, facilitating specific interactions with hydrophobic organelle like lipid droplets (LDs). Such a fluorescent molecular probe is ideally suited for elucidation of complex self-assembly processes and to decipher the intracellular dynamics of LDs. Invoking the concept, the main skeleton of 1,4-bis(1*H*-phenanthro[9,10-*d*]imidazol-2-yl)benzene abbreviated as BPIB, was functionalized with a varying number of octyl chains to obtain BPIB1 and BPIB2. The alkyl chains were crucial to circumvent the π-π stacking leading to the strong fluorescence in aggregates and solid-state. Contrary to BPIB and BPIB2, intermolecular interactions-driven spontaneous self-association of BPIB1 having an amine nitrogen center and a long alkyl chain resulted in a stimuli-responsive fluorescent organogel. We deciphered the reversible morphological transformation between supramolecular fibers and spherical nanoaggregates using fluorescence lifetime imaging microscopy. The gradual progression in the fluorescence lifetime provides a unique strategy in exploring the dynamics of the self-assembly process. Furthermore, BPIB1 was found to be a specific marker for LDs in multiple cell lines. The fluorescence correlation spectroscopy revealed the microenvironments near LDs. Highly photostable BPIB1 was employed for the real-time tracking of the LDs dynamics in live cells. Thus, a combined microscopic and spectroscopic approach demonstrated in the present study opens up new avenues for further exploration of intriguing molecular aggregation and intracellular dynamics.

INTRODUCTION

Intermolecular interactions-driven spontaneous self-association of molecular building units leads to diverse nano and microarchitectures.[1-3] In this context, a small change in molecular structure profoundly impacts supramolecular self-assembly.[4-7] As an example, a small modification in amino acid residues plays a crucial role in regulating the self-assembly and functional miscellany of natural macromolecules like peptides and proteins.[8,9] Inspired by natural systems, researchers have been exploring the delicate relationship of artificial self-assembled aggregates and their diverse physical, chemical, and biological properties.[3,10-18] A range of materials has been developed through the tiny change in molecular structures like single atom alteration, side-chain modifications, etc.[19-24] However, the fundamental understanding of the dynamics of self-assembly to tune the task-specific functions of molecular materials remains a challenge.

The molecular assembly process has a great impact on the size and shape of the aggregate structures and can be tuned through the variation of the local environments like polarity, the viscosity of the medium, and external stimuli like pH, temperature, and light.[7,25-31] In addition to the morphology, the optical properties of the self-assembled systems can be altered by engineering the specific functional units in π-conjugated small organic molecules.[25,32-34] Such morphology-dependent emissive organic aggregates receive a vital consideration owing to their applications in optoelectronic devices, sensors, and switches.[34-43] However, small strategic perturbations in the molecular structures for multifaceted function are intriguing. In this context, the integration of long alkyl chains into the rigid and π-conjugated molecular backbone prevents the π-π stacking in the aggregated state, resulting in enhanced fluorescence.[43-46] Additionally, the tuning of intermolecular interactions through the variation of alkyl chains may govern the nature of self-assembly, leading to various structures like particles, tubes, fibers, etc.[47-50] Moreover, the hydrophobicity of the alkyl chains improves the propensity of the probe to target the hydrophobic dynamic organelle like lipid droplets (LDs).[43,46,51]

The dynamics of LDs play a crucial role in diverse cellular activities, including protein sequestration and degradation and fatty acid trafficking.[52,53] Thus, the design and development of LD-markers have emerged as an exciting topic in current research.[54-56] The low photostability, less signal-to-noise ratio, and the tedious synthetic procedures of the commercial LD tracker dyes like Nile red, BODIPY 493/503 often pose a bottleneck in bioimaging.[57,58] Herein,

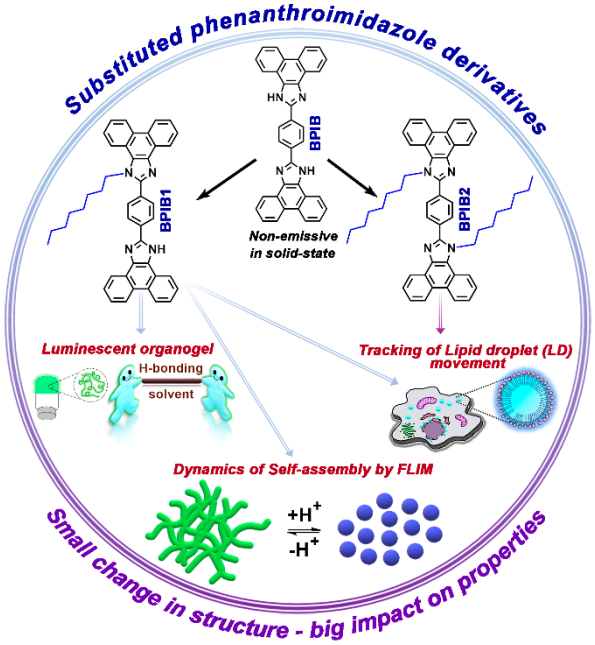

Figure 1. Schematic illustration depicting the strategic approach to achieve the multifunctional molecular materials through a small change in the chemical structure of BPIB [1,4-bis(1*H*-phenanthro[9,10-*d*]imidazol-2-yl)benzene]. The contrasting materials properties through tailoring the molecular structure: BPIB1: monoalkylated derivative, and BPIB2: dialkylated derivative compared to BPIB. The presence of both octyl chain and nitrogen centers in BPIB1 leads to solid-state optical switching, stimuli-responsive gelation, and lipid droplets (LDs) imaging.

we varied the number of octyl chains to develop π-conjugated substituted phenanthroimidazole-based multifunctional molecular materials (BPIB1: one octyl chain, and BPIB2: two octyl chains) exhibiting strong stimuli-responsive fluorescence in solution, aggregated, solid states and specific tracking of LDs. Unlike BPIB (no alkyl chains) and BPIB2, BPIB1 having an octyl chain and an amine nitrogen center formed an emissive organogel. Intriguing stimuli-responsive reversible morphological transformation of molecular aggregates was probed through fluorescence lifetime imaging microscopy (FLIM), a non-invasive technique,[59-61] allowing the precise description of the dynamics and the subtle changes of the microenvironment during the self-assembly process. The thermo-responsive gel-sol transformation was further explored for the white light emission. In addition, to direct the self-assembly, the hydrophobic octyl chain was found to be the key for targeting LDs. The highly photostable BPIB1 was employed in real-time tracking the dynamics of LDs in live cells.

RESULTS AND DISCUSSION

Blue fluorescent phenanthroimidazole derivative, 1,4-bis(1*H*-phenanthro[9,10-*d*]imidazol-2-yl)benzene (BPIB), is known to show high luminescence efficiency in solution due to the rigid and π-conjugated molecular structure.[62,63] However, fluorescence is completely diminished in the aggregated or solid-state. The optimized structure of BPIB showed the planar geometry, which could lead to the π-π stacking interactions in the aggregated state, quenching the

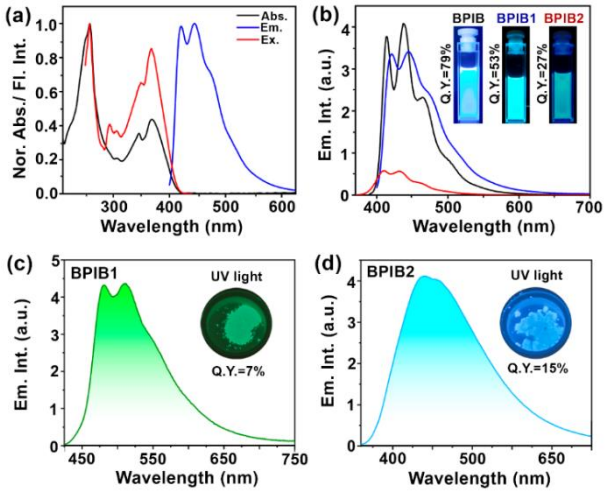

Figure 2. (a) Normalized absorption, emission (λ_{ex} = 375 nm) and excitation (λ_{em} = 450 nm) spectra of BPIB1 (5 μM) in toluene. (b) Comparative emission (λ_{ex} = 375 nm) profiles of BPIB, BPIB1 and BPIB2 in toluene (5 μM); insets: digital photographs of BPIB, BPIB1, and BPIB2 solutions in toluene under the illumination at 365 nm, fluorescence quantum yields (Q.Y.) are indicated. Solid-state emission spectra of (c) BPIB1 (λ_{ex} = 400 nm) and (d) BPIB2 (λ_{ex} = 400 nm) powder; inset: respective digital photographs of BPIB1, BPIB2 powder under the illumination at 365 nm, bright green (Q.Y. = 7 ± 0.5%) and blue (Q.Y. = 15 ± 3%) emission are observed from BPIB1 and BPIB2, respectively.

fluorescence. On the other hand, the presence of flexible octyl groups was the key reason to achieve the non-planar geometry for both BPIB1 and BPIB2. We anticipated that such angular geometry would reduce the π-π stacking in the aggregated state leading to the solid-state emission. Taking the inputs from the computational investigations, we synthesized a series of phenanthroimidazole-based derivatives (BPIB, BPIB1, and BPIB2) to elucidate the solid-state emission properties. 1,4-bis(1*H*-phenanthro[9,10-*d*]imidazol-2-yl)benzene (BPIB) was obtained through the condensation reaction between phenanthrene-9,10-quinone and terephthalaldehyde via a reported procedure with minor modifications.[62] BPIB1 and BPIB2 were synthesized through the substitution reaction of BPIB with 1-bromooctane in the presence of 1 and 2 equivalents of sodium hydride (NaH), respectively (Figure 1).

BPIB, BPIB1, and BPIB2 showed featured absorption and emission bands, typical for phenanthroimidazole-based chromophores (Figure 2a, 2b). The absorption peak maxima around 375 nm were due to the π-π* transition, resulting in the emission bands around 450 nm. The excitation spectrum was found to be similar to that of the absorption spectrum (Figure 2a). The increasing number of octyl chains decreased the fluorescence quantum yield in solution from 79% to 53% and 27% for BPIB to BPIB1 and BPIB2, respectively (Figure 2b), due to the activation of the nonradiative decay channels.[59]

Solid-state fluorescence and stimuli-responsive optical properties.

On the contrary to the trend of fluorescence quantum yield in solution, the presence of octyl chains was crucial for solid-state emission of BPIB1 and BPIB2 exhibiting

quantum yield of 7 ± 0.5% and 15 ± 3%, respectively (Figure 2c, 2d). As anticipated, BPIB was almost nonfluorescent in the solid-state due to the facile π-π stacking interactions. The non-planar geometry due to the presence of two octyl chains could reduce the π-π stacking interactions in BPIB2 more effectively, leading to the strongest emission among the three derivatives in the solid-state.

The lone pair of electrons on the nitrogen centers in BPIB, BPIB1, and BPIB2, are involved in conjugation and play a significant role in the stimuli-responsive optical properties. The protonation and deprotonation of the nitrogen centers of the BPIB series of molecules led to a reversible fluorescence switching (Figure 3a). The strong cyan emission from the BPIB1 (5 μM, toluene) coated nonfluorescent silica plate under the illumination at 365 nm was changed to yellowish-green upon exposing to the saturated trifluoroacetic acid (TFA) vapor for 10 s due to the protonation (Figure 3b). The gradual fluorescence color change could be due to the sequential protonation of imine nitrogen centers in BPIB1. The highest occupied and lowest unoccupied molecular orbitals (HOMO and LUMO) distributions in the mono and di-protonated forms of BPIB1 showed the possibility of intramolecular charge transfer (ICT). Evidently, a red shift with reduced intensity in the emission spectra was noticeable when the protonation was carried out in DMSO as compared to toluene, indicating the ICT behaviour in protonated BPIB1. The reversible switching between cyan and yellowish-green fluorescence of BPIB1-silica plate upon consecutive exposure to TFA (10 s) and triethylamine (TEA, 10 s) vapor was found to be fatigue-resistant and repeatable for multiple cycles (Figure 3b).

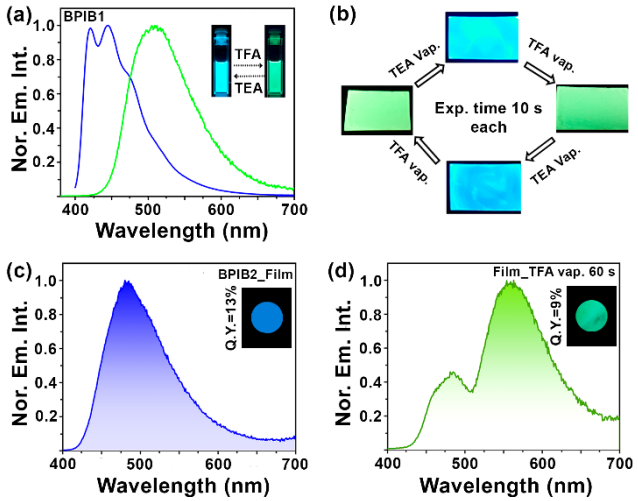

Figure 3. (a) Fluorescence spectra of BPIB1 in dimethyl sulfoxide (5 μM) and with the addition of trifluoroacetic acid (TFA, pH ~ 2); inset: respective digital photographs of BPIB1 solution upon addition of TFA and triethylamine (TEA) under illumination at 365 nm. (b) Nonfluorescent silica-coated thin layer chromatography plates were dipped into BPIB1 solution in dimethyl sulfoxide (5 μM) and consecutively exposed (Exp.) to TFA and TEA vapor (10 s), reversible fluorescence switching for multiple cycles was noticeable through the digital photographs obtained under the illumination of UV light at 365 nm. Solid-state emission spectra (λ_{ex} = 390 nm) and fluorescence quantum yields (Q.Y.) of the drop-casted thin film of BPIB2 on quartz plate (50 μL, 5 μM chloroform solution, dried under vacuum): (c) pristine film, (d) film exposed to TFA vapor for 60 s; insets: respective digital photographs under the illumination at 365 nm.

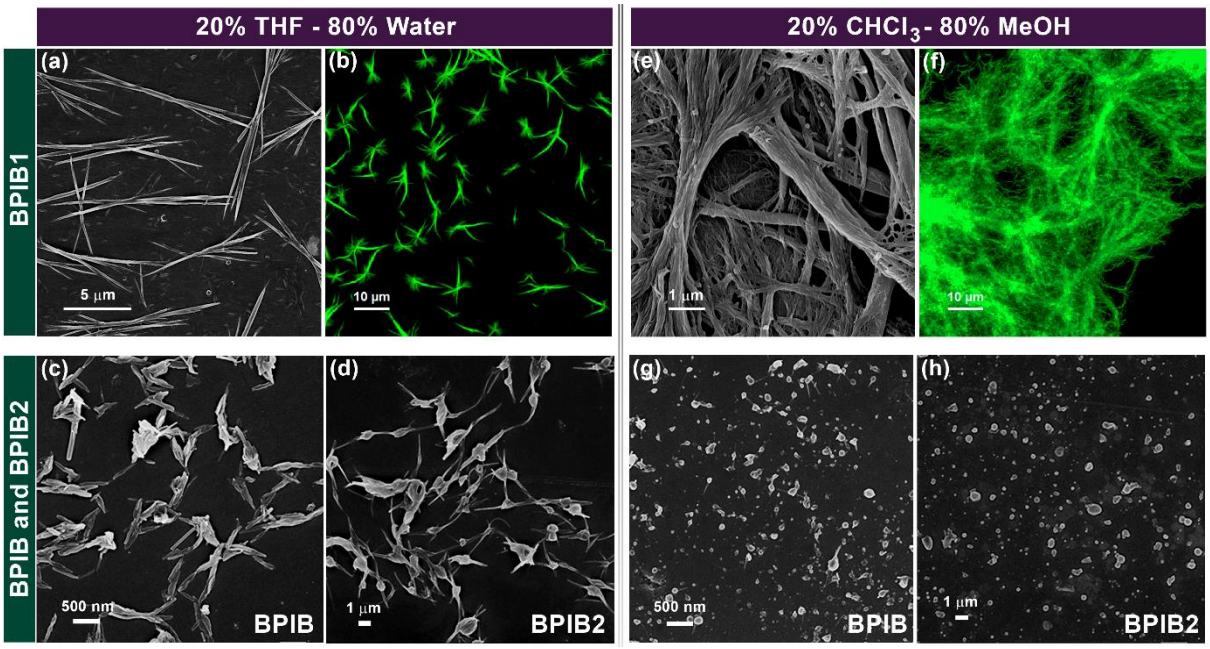

Figure 4. (a) The field emission scanning electron microscopy (FESEM), and (b) confocal laser scanning microscopy (CLSM) images of BPIB1 (10 μM) in the THF-water mixture having a water content of 80% illustrating the formation of anisotropic nanofibers. FESEM images of (c) BPIB (10 μM), (d) BPIB2 (10 μM) in THF-water mixture having the water content of 80%. (e) FESEM, and (f) CLSM images of BPIB1 gel (1 mM, 20% $CHCl_3$ and 80% MeOH). FESEM images of (g) BPIB (1 mM), and (h) BPIB2 (1 mM) in 20% $CHCl_3$ and 80% MeOH mixture. 10 μL respective dispersion were drop-casted on Si wafer and dried under vacuum to prepare the samples for FESEM.

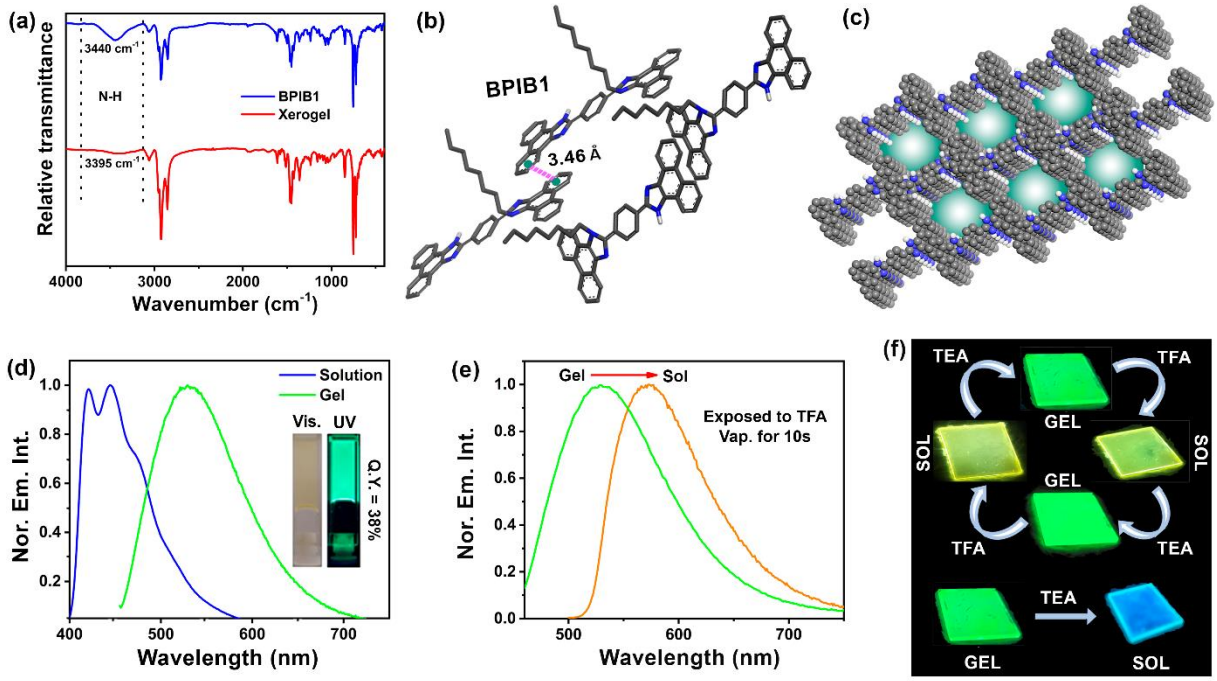

Figure 5. (a) Fourier transform infrared spectroscopy of BPIB1 powder (blue) and BPIB1 xerogel (red). (b) Molecular packing showing the π-π interactions (3.46 Å) between two BPIB1 molecules of adjacent unit cells. The unit cell was obtained through the Pawley refinement of powder X-ray diffraction data using Materials Studio 6.1. (c) The representation of the three-dimensional supramolecular assembly of BPIB1 through CPK (Corey-Pauling-Koltun) space-filling model; the void space facilitates the intermolecular hydrogen bonding with low molecular weight alcohols leading to the formation of a supramolecular gel. Color code: C = grey, H = white, and N = blue. (d) Comparative emission profiles of BPIB1 in the form of solution ($CHCl_3$: 5 μM; λ_{ex} = 375 nm) and gel (1 mM, 20% $CHCl_3$ and 80% MeOH; λ_{ex} = 450 nm). Inset: the digital photographs of green-emissive BPIB1 gel (Q.Y. = 38%) under visible light and the illumination at 365 nm. (e) Emission spectra of the thin film made by BPIB1 gel (λ_{ex} = 450 nm) and the film exposed to TFA vapor for 10 s (λ_{ex} = 490 nm). The gel to sol transformation is due to the protonation of the amine nitrogen center. (f) Digital photographs of the native thin film made by BPIB1 gel and the same film was exposed to trifluoroacetic acid (TFA) and triethylamine (TEA) vapor for 10 s under illumination at 365 nm.

On the other hand, the high fluorescence quantum yield of BPIB2 prompted us to check the optical switchability in the drop-casted thin film on a quartz plate. The pristine film showed a blue emission with a peak maximum of 475 nm (Figure 3c). A redshift in the emission spectra was noticeable while exposing the film to TFA vapor for 15 s. A new emission band at 550 nm was observed due to the protonation of BPIB2 upon 30 s exposure to TFA vapor. The 550 nm peak was further intensified with respect to the peak at 475 nm (neutral BPIB2) and reached saturation at 60 s (Figure 3d). On deprotonation, green to blue fluorescence switching was affected by exposing the acidified thin film to TEA vapor for 60 s.

Probing the dynamics of supramolecular gel formation.

Strong emission of BPIB1 and BPIB2 in solution and solid-state impelled us to explore their emission in the binary solvent mixture. A systematic study in the THF-water mixture revealed the formation of green and blue emissive aggregates for BPIB1 and BPIB2, respectively, with increasing water fractions. The field emission scanning electron microscopy (FESEM) images showed the formation of nanofibers of BPIB1 in the THF- water mixture having a water content of ≥ 80% (Figure 4a). Figure 4b shows the confocal laser scanning microscopy (CLSM) image of BPIB1 in the THF-water mixture with a water content of 80%. In contrast, BPIB and BPIB2 mostly formed irregular-shaped particles in THF-water (20%-80%) mixture (Figure 4c, 4d).

The supramolecular gelation was observed serendipitously in 20% $CHCl_3$ and 80% MeOH at a specific concentration (1 mM) while exploring the intriguing self-assembly behavior of BPIB1. The FESEM and CLSM images of BPIB1 gel showed a network of intensely green fluorescent nanofibers (Figure 4e, 4f). The gel formation was only possible in the presence of a polar protic solvent, mostly with lower aliphatic alcohols. On the contrary, BPIB (no octyl chain) and BPIB2 (no amine nitrogen centers) were found to be aggregated in the form of nanoparticles in 20% $CHCl_3$ and 80% MeOH (Figure 4g, 4h). Further, the monosubstitution of BPIB with smaller alkyl chains like butyl [BPIB1 (4)] or hexyl [BPIB1 (6)] did not yield gelation. Thus, the results suggested the role of both octyl chain and amine 'N' center for the formation of BPIB1 gel. Fourier transform infrared (FTIR) spectra showed a weak band at ~ 3395 cm^{-1} compared to an intense band at ~ 3440 cm^{-1} for xerogel and pristine BPIB1 powder, respectively (Figure 5a). The shift of -NH stretching frequency and a lower intensity indicated the presence of intermolecular interactions through amine nitrogen in the supramolecular gel matrix.

Further, noncovalent interactions-driven supramolecular gel formation was explored through molecular modeling studies. The unit cell parameters of BPIB1 (a = 15.07 Å, b = 7.40 Å, c = 14.02 Å, and α = 90°, β = 106.6°, γ = 90°) and BPIB2 (a = 17.0 Å, b = 7.23 Å, c = 14.69 Å, and α = 90°, β =

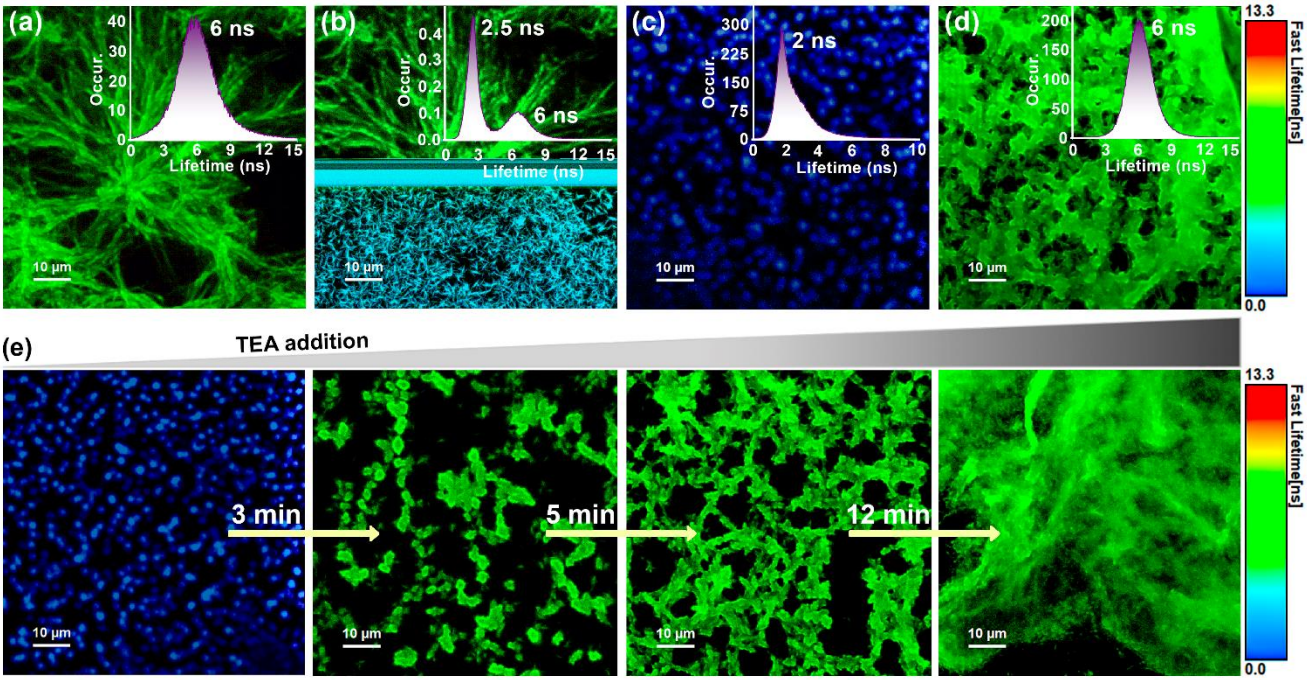

Figure 6. Fluorescence lifetime imaging (FLIM) of (a) pristine BPIB1 gel (1 mM, 20% $CHCl_3$ and 80% MeOH), (b) BPIB1 gel with the addition of trifluoroacetic acid (TFA; 1 µL; acid was added during the image capturing process, the middle region of the image signifies the auto adjustment of the focus due to the spontaneous transformation of emissive gel to sol), (c) complete formation of BPIB1 sol, and (d) BPIB1 gel after addition of triethylamine (TEA; 1 µL) to the acidified sol; inset: corresponding fluorescence lifetime histograms demonstrating reversible gel-sol-gel transformation; the average lifetime of gel (~ 6 ns), sol (~ 2 ns), and the mixture of sol-gel are indicated. (e) Morphological transformation during sol to gel transformation upon addition of 1 µL of TEA in an acidified sol of BPIB1 elucidated through real-time FLIM images. The green and blue colors in the images refer to fluorescence lifetime distribution. Scale = 10 µm.

129.6°, γ = 90°) were obtained through the experimental powder X-ray diffraction (PXRD) pattern corroborating with the Pawley refined profile using Materials Studio 6.1 package.[7] The unit cell packing showed the π-π stacking interactions between two BPIB1 molecules of the adjacent unit cells (Figure 5b). Figure 5c represents the π-π stacking interactions-driven three-dimensional supramolecular array formation of BPIB1. The void space in such a self-assembled structure could accommodate the low molecular weight alcohols like methanol, ethanol through the hydrogen bonding interactions with the basic nitrogen centers of BPIB1, leading to the formation of the gel. On the contrary, no gel formation was observed under similar conditions for BPIB2 having two long alkyl chains, preventing π-π stacking interactions.

The supramolecular self-assembly led to a red shift in the emission spectra for the BPIB1 gel compared to the solution (Figure 5d). The fluorescence quantum yield of the green emissive gel was found to be 38% (Figure 5d; inset). The similar emission spectra with λ_{max}^{em} = 530-550 nm indicated the comparable nature of supramolecular assembly in solid, dispersion, and gel matrices. As the amine 'N' would take part in the gel formation, the protonation or deprotonation could disrupt the 3D network. Evidently, the gel-coated thin film on a quartz plate, upon exposure to TFA vapor for 10 s, transformed to sol due to the protonation of BPIB1. The emission spectrum of the sol was found to be red-shifted as compared to that of the BPIB1 gel (Figure 5e). A reversible sol to gel transformation was noticeable due to the deprotonation upon exposing the quartz plate to TEA vapor for 10 s (Figure 5f). The stimuli-responsive reversible transformation between gel and sol was found to be repeatable for multiple cycles (Figure 5f). On the contrary, a blue emission was noticed for the gel to sol transformation upon exposure of TEA vapor to gel-coated thin film for 10 s due to the deprotonation of amine nitrogen of BPIB1 (Figure 5f). The blue emission quite resembled the spectrum of BPIB1 in the presence of TEA in the solution. Such blue emission was due to the twisting in the molecular structure, which reduced the π-electron communication in the deprotonated form of BPIB1.

We carried out fluorescence lifetime imaging microscopy (FLIM) to obtain temporally and spatially resolved fluorescence profiles in order to gain more insight into the molecular self-assembly processes during the reversible sol-gel transformation (Figure 6). The spontaneous transformation of gel to sol with distinct morphological variation was observed in the FLIM images upon addition of TFA (1 µM, 1 µL) to the pristine BPIB1 gel (Figure 6a-d). The broad feature in the fluorescence lifetime histogram for pristine gel indicated the heterogeneity in the system (Figure 6a, inset). On the other hand, the fluorescence lifetime histogram exhibited two distinct peaks with maxima at ~ 6 and ~ 2.5 ns due to the gel and the sol, respectively, for the acidified sample indicating a phase transition (Figure 6b, inset). The complete conversion of gel to sol led to a distinct variation of morphology from connected fibers to segregated near-spherical particles, as revealed through the FLIM images (Figure 6a and 6c). The

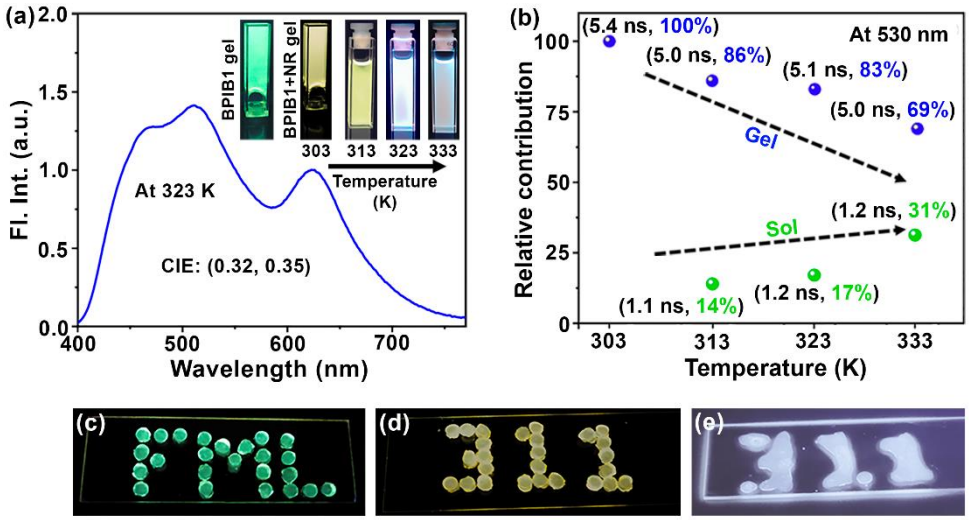

Figure 7. (a) Emission spectra of the white light emitting BPIB1+Nile red (NR) gel at 323 K. The Commission Internationale de l'Eclairage (CIE) value is mentioned. Insets: the digital photographs of BPIB1 gel and BPIB1+NR gel with the variation of the temperature (303 K to 333 K). (b) The relative contribution of the emission decay times monitored at 530 nm with the variation of temperature from 303 K to 333 K depicting gel to sol transformation. The digital photographs of fluorescent patterns fabricated using (c) BPIB1 gel, (d) BPIB1+NR gel at 303 K, and (e) BPIB1+NR gel at 323 K under the illumination of UV light (λ_{ex} = 365 nm).

morphological transformation due to the sol formation was corroborated with a sharp feature band in the lifetime histogram with a maximum at 2 ns (Figure 6c, inset).

The reverse phenomenon of a sol to gel transformation upon addition of TEA (1 μM, 1 μL) to the acidified sol was also probed through FLIM images (Figure 6d). The lifetime histogram reflected a similar result, like in the case of pristine gel with a fluorescence lifetime of 6 ns (Figure 6d, inset). However, the variation of the width of lifetime histograms of the pristine gel and the resultant gel after acid-base treatment suggested a difference in microheterogeneity also reflected through the difference in morphology (Figure 6a and 6d). We further monitored the fluorescence decay profiles during the FLIM measurements. The average decay time obtained from both FLIM and macroscopic cuvette-based experiments was corroborated well with that obtained from the fluorescence lifetime histograms. Further, the intriguing morphological evolution and the step-wise aggregation process leading to the supramolecular gelation was deciphered through FLIM (Figure 6e), which has rarely been explored so far in the context of dynamic self-assembly.

The new physical insights behind the contrasting stimuli-responsive fluorescence encouraged us to explore the BPIB1 gel matrix as a versatile platform for temperature-dependent tunable fluorescence, including white light emission. The green emission of the pristine BPIB1 gel was found to be shifted in the blue region (λ_{em} ~ 450 nm, similar to BPIB1 solution) with increasing temperature. The encapsulation of Nile red led to the change in fluorescence of BPIB1 gel from green to yellow at room temperature. The gradual formation of blue emissive sol upon increasing the temperature of Nile red embedded BPIB1 gel resulted in a nearly pure white light emission at 323 K with Commission Internationale de l'Eclairage (CIE) coordinates (0.32, 0.35) due to the additive mixing of three primary colors (Figure 7a). A further increase in temperature caused a predominant bluish-white emission, leading to cool white light (CIE: 0.28, 0.32).

Further, the fluorescence lifetime decay measurements at 530 nm (gel emission) revealed the dynamics of gel to sol transformation with increasing temperature (Figure 7b). A gradual decrease in the relative contribution for the gel decay time and a concomitant increase of the same for the sol indicated the disruption of the gel network with

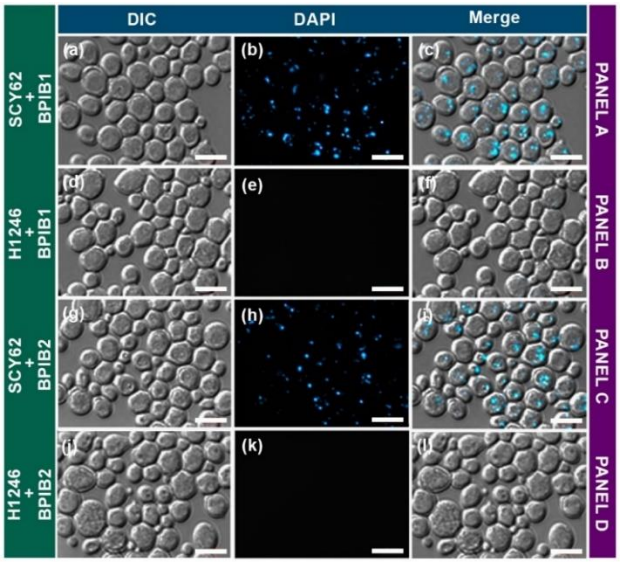

Figure 8. Microscopy images of *Saccharomyces cerevisiae* (budding yeast) incubated with BPIB1 and BPIB2 at 30 °C for 30 mins: panel A: wild-type yeast cells (SCY62) incubated with BPIB1, panel B: lipid droplets (LDs)-deficient yeast cells (H1246) incubated with BPIB1, panel C: wild-type yeast cells (SCY62) incubated with BPIB2, and panel D: LD-deficient yeast cells (H1246) incubated with BPIB2; (a, d, g, j) differential interference contrast (DIC) images, (b, e, h, k) fluorescent images with the DAPI filter (blue channel, λ_{ex} = 335-383 nm, λ_{em} = 420-470 nm, BPIB1 or BPIB2 emission), and (c, f, i, l) merged fluorescent images. Scale = 2 μm.

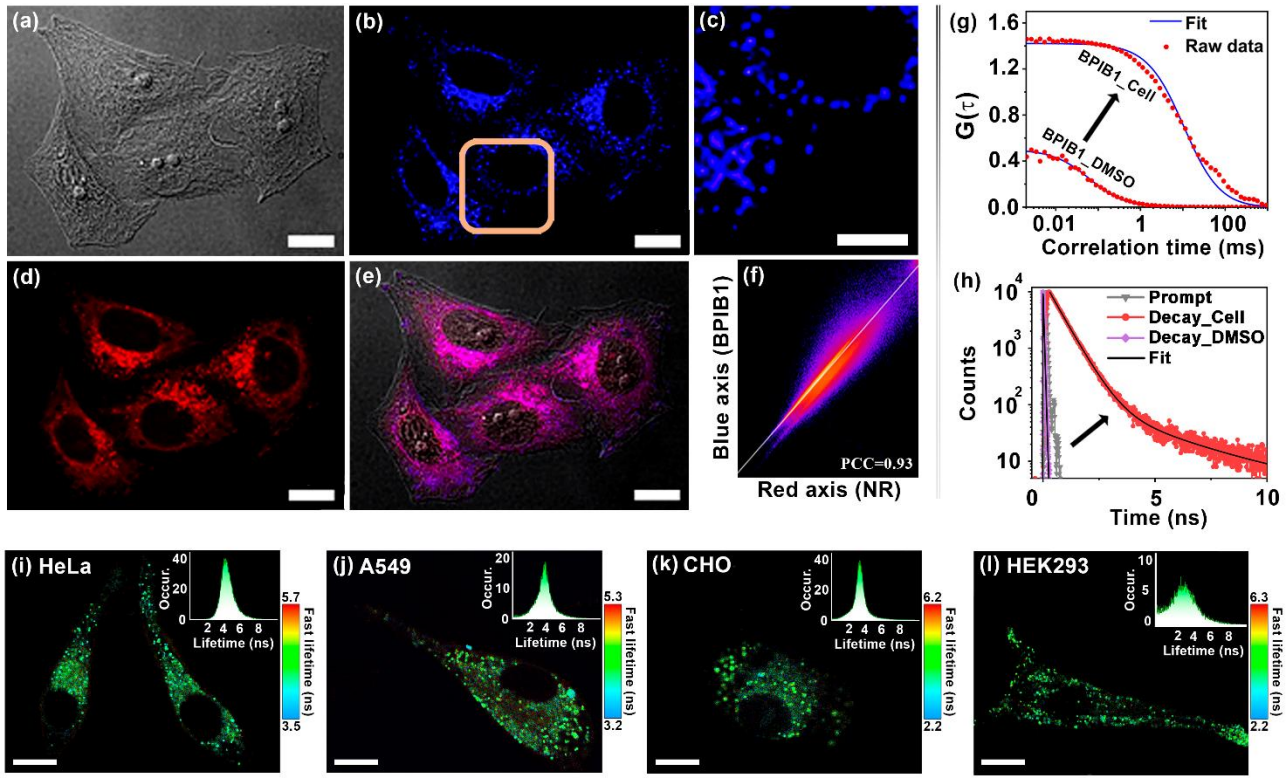

Figure 9. Microscopy images of HeLa cells costained with BPIB1 and Nile red. (a) DIC image, (b) fluorescent image obtained with a DAPI filter (blue channel, λ_{ex} = 335-383 nm, λ_{em} = 420-470 nm), (c) enlarge view depicting punctate dot-like pattern of LD-staining, (d) fluorescent image obtained with a DsReD filter (red channel, λ_{ex} = 538-562 nm, λ_{em} = 570-640 nm), (e) merged fluorescent image of BPIB1 and Nile red depicting colocalization in LDs, and (f) Pearson's correlation of BPIB1 and Nile red intensities (correlation coefficient: 0.93). (g) FCS traces of BPIB1 (5 nM) in DMSO and BPIB1 (50 nM) inside the LDs in Hela cells. (g) Fluorescence lifetime decay profiles of BPIB1 (5 nM) in DMSO and BPIB1 (50 nM) inside the LDs in Hela cells. Fluorescence lifetime imaging (FLIM) of live (i) HeLa, (j) A549, (k) CHO, and (l) HEK293 cells stained with BPIB1 (50 nM) at 30 °C for 10 mins, λ_{ex} = 405 nm, λ_{em} = 427-488 nm. Inset: corresponding fluorescence lifetime histograms demonstrating the versatility of BPIB1 for the imaging of LDs in multiple cell lines. Scale = 10 μm.

increasing temperature (Figure 7b). Additionally, the temperature-dependent emission switching was invoked for the fabrication of different fluorescent patterns (Figure 7c-e). The heating of the '311' pattern at 323 K led to white light emission (Figure 7e).

Imaging and tracking of lipid droplets (LDs).

The long octyl chain in BPIB1 and BPIB2 makes both the dyes hydrophobic in nature.[46] Hence, it was anticipated that both the dyes could localize to lipid-enriched subcellular organelles, like lipid droplets (LDs), through hydrophobic interactions.[43,44,51] In this context, we explored BPIB1 and BPIB2 as LD-specific probes in *Saccharomyces cerevisiae* (budding yeast) and mammalian cell lines. An amenable yet powerful model system, budding yeast provides an easy platform for genetic manipulation. Owing to high conservation between yeast and mammalian cells in the lipolytic process, studies on the LDs in yeast may share a direct relevance with the mammalian system. Spot test assay and growth curve analysis of yeast cells suggested BPIB1 and BPIB2 as suitable nontoxic probes for subcellular imaging. Fluorescence microscopy images of BPIB1 and BPIB2-stained yeast cells revealed a punctate dot-like pattern (Figure 8, panels A, C). Further, staining of LD-deficient quadruple mutant *(Δdga1*, *Δlro1*, *Δare1*, and *Δare2)* yeast cells indicated the punctate structures only in wild type (Figure 8, panel A, C), but not in the mutant cells (Figure 8, panel B, D). Additionally, the costaining of LDs extracted from yeast cells suggested the specificity of BPIB1 and BPIB2 towards LDs. The colocalization studies employing the Nile red (a commercial LD tracker), MitoTracker Red, and LysoTracker Red unambiguously ascertained the specific localization of BPIB1 and BPIB2 in LDs.

We further employed BPIB1 for mammalian cell imaging due to its better solubility in polar solvents like dimethyl sulfoxide and higher fluorescent quantum yield compared to BPIB2. MTT assay of HeLa cells indicated 80% viability for BPIB1 at 90 nM. The fluorescence microscopy images showed a punctate dot-like pattern in the cytoplasm due to the staining of LDs by BPIB1 (Figure 9a-c). The colocalization studies with Nile red revealed the Pearson's coefficient of colocalization (PCC) of 0.93 (Figure 9d-f). Further, the spectroscopic features of BPIB1 in live cells were probed using fluorescence correlation spectroscopy (FCS) and fluorescence lifetime imaging (FLIM) through a time-resolved confocal microscope. The FCS traces showed an increase in the diffusion time (τ_d) of BPIB1 in LDs as compared to that in solution (Figure 9g). The local viscosity in LDs was calculated through τ_d values using the equation S3 and was found to be ~ 37 cP. Similarly, the average fluorescence decay time of BPIB1 was found to be 4.5 ns in

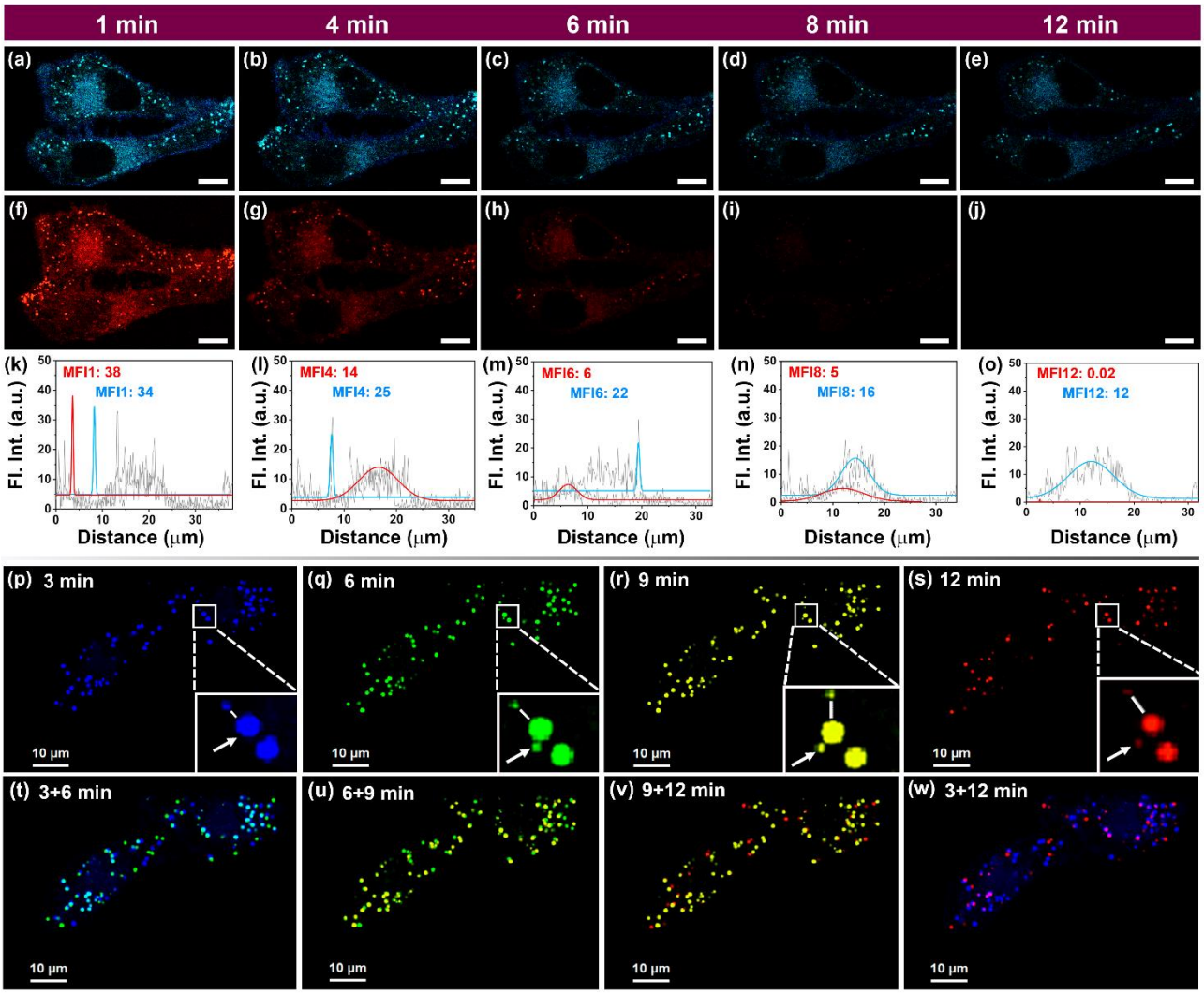

Figure 10. Confocal laser scanning microscopy (CLSM) images of live HeLa cells costained with BPIB1 (50 nM) and Nile red (50 nM) at 30 °C for 10 mins with increasing scanning time under constant laser irradiation. Images of HeLa cells stained with (a-e) BPIB1 (λ_{ex} = 405 nm, λ_{em} = 428-488 nm), and (f-j) Nile red (λ_{ex} = 540 nm, λ_{em} = 580-670 nm) suggesting greater photostability of BPIB1; Scale = 10 μm. All the images were captured for 30 s scanning time. (k-o) Comparative intracellular intensity plots of BPIB1 and Nile red with increasing scanning time, k: 1 min, l: 4 min, m: 6 min, n: 8 min, o: 12 min; the mean fluorescence intensity (MFI) with photoirradiation time is indicated. (p-s) Real-time tracking of LDs dynamics using BPIB1 as a marker; different pseudo-colors used to display the movement of LDs at different time points (λ_{ex} = 405 nm; λ_{em} = 428-488 nm); insets (p-s): zoomed view of specific regions. (t-w) The merged images at two different time points confirming the dynamics of LDs. Scale = 10 μm.

the HeLa cells (Figure 9h). The diffusion time and average fluorescence decay time increased due to the internalization of BPIB1 in LDs through hydrophobic interactions.

We further employed multiple cancerous cell lines for LD imaging as the abundance of LDs is significantly higher in cancer cells due to a faster lipid metabolism compared to normal cells.[52,53,64] The fluorescence lifetime images ascertained BPIB1 as an LD marker for HeLa, A549, CHO, and HEK293 cells (Figure 9i-l). The diverse distribution and heterogeneity of LDs in different cell lines were reflected by the difference in the width of the lifetime histograms. The variation of lifetime distribution could be due to the difference in the interactions of BPIB1 with LDs in multiple cell lines (inset; Figure 9i-l).

The dynamic nature of the LDs has a great impact on several biological functions like cellular metabolism.[52,65] Thus, the tracking of the LDs is crucial, albeit challenging, and only a few reports are available to date.[64,66-68] A highly photostable LD tracker dye is desirable to monitor the dynamics of the LDs over time. The intracellular photostability of BPIB1 was studied using confocal laser scanning microscopy and was compared with Nile red (Figure 10a-o). The HeLa cells, costained with BPIB1 and Nile red, were exposed to continuous irradiation at 405 nm and 540 nm, respectively, under identical conditions. The higher photostability of BPIB1 over Nile red was evident (Figure 10a-o). The gradual decrease of fluorescence intensity was observed from 6 min onwards for Nile red (Figure 10f-j). On the contrary, an appreciable signal was obtained using BPIB1 even at 12 min of continuous laser irradiation (Figure 10e). Additionally, the plot of intracellular fluorescence intensity vs. distance with the laser irradiation time and the mean fluorescence intensity

(MFI) values also showed the high photostability of BPIB1, desirable for real-time bioimaging (Figure 10k-o).

The low cytotoxicity, high specificity, and enhanced photostability encouraged us to employ BPIB1 for tracking the LDs dynamics in live HeLa cells. The spatial distribution of LDs over time could be easily identified through a close inspection of Figure 10p-s. Additionally, a Movie, compiled of a series of fluorescent images of LDs with different time intervals for 30 minutes, depicted the dynamics of LDs in HeLa cells. Further, we represented the CLSM images with different pseudocolors of blue (3 min), green (6 min), yellow (9 min), and red (12 min) to distinguish the spatial distribution of LDs (Figure 10p-s). The merged images at two different time points [(3+6 min), (6+9 min), (9+12 min), and (3+12 min)] ascertained the movement of the LDs over time (Figure 10t-w). Moreover, the close inspection of Figure 10p-s distinctly shows the dynamic motion, including fission, fusion processes, and the changes in the size of LDs over time.

CONCLUSION

In conclusion, we demonstrated the impact of small strategic perturbations in the molecular structures to tune the morphology of the self-assembled aggregates and their diverse physical, chemical, and biological properties. The intermolecular interactions-driven self-assembly pathways leading to stimuli-responsive reversible BPIB1 gel (fibers) to sol (spherical nanoaggregates) with contrasting morphological evolution were explored through fluorescence lifetime imaging microscopy. The spectroscopic, microscopic, and computational investigations implied the influence of both the amine nitrogen and the long octyl chain towards the formation of a supramolecular gel. Further, fine-tuning of the gelation process resulted in temperature-dependent white light emission. The presence of the hydrophobic octyl chains led to BPIB1 and BPIB2 as specific markers for lipid droplets. Additionally, the microenvironment near lipid droplets was probed through fluorescence correlation spectroscopy and fluorescence lifetime imaging microscopy, revealing the diverse distribution and heterogeneity of lipid droplets in different cell lines. The highly photostable BPIB1 was employed to track the dynamics of lipid droplets. Thus, exploring stimuli-responsive reversible molecular assembly and intracellular dynamics by time-resolved spectroscopic and microscopic approaches provides further avenues for deciphering the evolution process and regulating the functions of a diverse range of biologically relevant supramolecular self-assembled structures.

Funding Sources

Financial support from BRNS, DAE (No. 37(2)/14/06/2016BRNS/ 37020), and the Council of Scientific and Industrial Research (CSIR), New Delhi (No. 01(2878)/17/EMR-II).

AUTHOR INFORMATION

Corresponding Author

***Abhijit Patra**: Department of Chemistry, Indian Institute of Science Education and Research Bhopal, Bhopal By-Pass Road, Bhauri, Bhopal 462066, Madhya Pradesh, India; http://orcid.org/0000-0003-3144-1813;*
Email: abhijit@iiserb.ac.in

Raghuvir Singh Tomar: *Department of Biological Sciences, Indian Institute of Science Education and Research Bhopal, Bhopal By-Pass Road, Bhauri, Bhopal 462066, Madhya Pradesh, India;*
Email: rst@iiserb.ac.in

Authors

Subhankar Kundu: *Department of Chemistry, Indian Institute of Science Education and Research Bhopal, Bhopal By-Pass Road, Bhauri, Bhopal 462066, Madhya Pradesh, India; http:// orcid.org/0000-0001-9294-5551;*
Email: subhankar16@iiserb.ac.in

Bahadur Sk: *Department of Chemistry, Indian Institute of Science Education and Research Bhopal, Bhopal By-Pass Road, Bhauri, Bhopal 462066, Madhya Pradesh, India; https://orcid.org/0000-0002-7098-5429;*
Email: bahadursk@yahoo.com

Nitu Saha: *Department of Biological Sciences, Indian Institute of Science Education and Research Bhopal, Bhopal By-Pass Road, Bhauri, Bhopal 462066, Madhya Pradesh, India;*
Email: nitu@iiserb.ac.in

Tapas Kumar Dutta: *Department of Chemistry, Indian Institute of Science Education and Research Bhopal, Bhopal By-Pass Road, Bhauri, Bhopal 462066, Madhya Pradesh, India; https://orcid.org/0000-0001-6431-2060;*
Email: tapas17@iiserb.ac.in

Subhadeep Das: *Department of Chemistry, Indian Institute of Science Education and Research Bhopal, Bhopal By-Pass Road, Bhauri, Bhopal 462066, Madhya Pradesh, India; https://orcid.org/0000-0002-3588-3726;*
Email: subhadeep19@iiserb.ac.in

ACKNOWLEDGMENT

Infrastructural support from IISERB and the financial support from BRNS, DAE (No. 37(2)/14/06/2016BRNS/ 37020), and the Council of Scientific and Industrial Research (CSIR), New Delhi (No. 01(2878)/17/EMR-II) are gratefully acknowledged. We thank Sten Stymne for providing LD-deficient quadruple mutant. SK thanks UGC for the fellowship. BSk, NS, TKD, and SD acknowledge IISERB for the fellowship. SK thank Mr. Arkaprabha Giri and Dr. MD. Waseem Hussain, for the fruitful suggestions.

REFERENCES

1. Philp, D.; Stoddart, J. F. Self-Assembly in Natural and Unnatural Systems. *Angew. Chem. Int. Ed*. **1996**, *35*, 1154.
2. Whitesides, G. M.; Grzybowski, B. Self-Assembly at All Scales. *Science* **2002**, *295*, 2418.
3. Stupp, S. I; Palmer, L. C. Supramolecular Chemistry and Self-Assembly in Organic Materials Design. *Chem. Mater*. **2014**, *26*, 507.
4. Kulkarni, C.; Meijer, E. W; Palmans. A. R. A. Cooperativity Scale: A Structure-Mechanism Correlation in the Self-Assembly of Benzene-1,3,5-tricarboxamides. *Acc. Chem. Res*. **2017**, *50*, 1928.
5. Ochs, N. A. K.; Lewandowska, U.; Zajaczkowski, W.; Corra, S.; Reger, S.; Herdlitschka, A.; Schmid, S.; Pisula, W.; Mullen, K.; Bauerle, P.; Wennemers, H. Oligoprolines Guide the Self-Assembly of Quaterthiophenes. *Chem. Sci*. **2019**, *10*, 5391.
6. Knaapila, M.; Dias, F. B.; Garamus, V. M.; Torkkeli, L. A. M.; Leppänen, K.; Galbrecht, F.; Preis, E.; Burrows, H. D.; Scherf, U.;

Monkman. A. P. Influence of Side Chain Length on the Self-Assembly of Hairy-Rod Poly(9,9-dialkylfluorene)s in the Poor Solvent Methylcyclohexane. *Macromolecules* **2007**, *40*, 9398.
7. Kundu, S.; Chowdhury, A.; Nandi, S.; Bhattacharyya, K.; Patra, A. Deciphering the Evolution of Supramolecular Nanofibers in Solution and Solid-State: A Combined Microscopic and Spectroscopic Approach. *Chem. Sci*. **2021**, *12*, 5874.
8. Zou, R.; Wang, Q.; Wu, J.; Wu, J.; Schmuck, C.; Tian, H. Peptide Self-Assembly Triggered by Metal Ions. *Chem. Soc. Rev*. **2015**, *44*, 5200.
9. Hendricks, M. P.; Sato, K.; Palmer, L. C.; Stupp, S. I. Supramolecular Assembly of Peptide Amphiphiles. *Acc. Chem. Res*. **2017**, *50*, 2440.
10. Lehn, J. -M. Supramolecular Chemistry-Scope and Perspectives Molecules, Supermolecules, and Molecular Devices. *Angew. Chem. Int. Ed*. **1988**, *27*, 89.
11. Ajayaghosh, A.; George, S. J. First Phenylenevinylene Based Organogels: Self-Assembled Nanostructures Via Cooperative Hydrogen Bonding and π-Stacking. *J. Am. Chem. Soc*. **2001**, *123*, 5148.
12. Chakrabarty, R.; Mukherjee, P. S.; Stang, P. J. Supramolecular Coordination: Self-Assembly of Finite Two- and Three-Dimensional Ensembles. *Chem. Rev*. **2011**, *111*, 6810.
13. McEntee. G. J.; Vilela. F.; Skabara. P. J.; Anthopoulos. T. D.; Labram. J. G.; Tierney. S.; Harringtond. R. W.; Clegg. W. J. Self-assembly and charge transport properties of a benzobisthiazole end-capped with dihexyl thienothiophene units. *J. Mater. Chem*. **2011**, *21*, 2091.
14. Silva, R. M. D.; Zwaag, D.; Albertazzi, L.; Lee, S.; Meijer, E. W.; Stupp, S. I. Super-Resolution Microscopy Reveals Structural Diversity in Molecular Exchange Among Peptide Amphiphile Nanofibres. *Nat. Commun*. **2016**, *7*, 11561.
15. Xing, P.; Zhao. Y. Multifunctional Nanoparticles Self-Assembled from Small Organic Building Blocks for Biomedicine. *Adv. Mater*. **2016**, *28*, 7304.
16. Lossada, F.; Hoenders, D.; Guo, J.; Jiao, D.; Walther, A. Self-Assembled Bioinspired Nanocomposites. *Acc. Chem. Res*. **2020**, *53*, 2622.
17. Shen, C.; Bialas, D.; Hecht, M.; Stepanenko, V.; Sugiyasu, K.; Würthner, F. Polymorphism in Squaraine Dye Aggregates by Self-Assembly Pathway Differentiation: Panchromatic Tubular Dye Nanorods versus J-Aggregate Nanosheets. *Angew. Chem. Int. Ed*. **2021**, *60*, 11949.
18. Li, R.; Tessarolo, J.; Lee, H.; Clever, G. H. Multi-stimuli Control over Assembly and Guest Binding in Metallosupramolecular Hosts Based on Dithienylethene Photoswitches. *J. Am. Chem. Soc*. **2021**, *143*, 3865.
19. Balakrishnan, K.; Datar, A.; Naddo, T.; Huang, J.; Oitker, R.; Yen, M.; Zhao, J.; Zang, L. Effect of Side-Chain Substituents on Self-Assembly of Perylene Diimide Molecules: Morphology Control. *J. Am. Chem. Soc*. **2006**, *128*, 7390.
20. Stals, P. J. M.; Haveman, J. F.; Rapu´n, R. M.; Fitie´, C. F. C.; Palmans. A. R. A.; Meijer, E. W. The Influence of Oligo(ethylene glycol) Side Chains on the Self-Assembly of Benzene-1,3,5-tricarboxamides in the Solid State and in Solution. *J. Mater. Chem*. **2009**, *19*, 124.
21. Chen, Z.; Fimmel, B.; Würthner, F. Solvent and Substituent Effects on Aggregation Constants of Perylene Bisimide π-Stacks-a Linear Free Energy Relationship Analysis. *Org. Biomol. Chem*. **2012**, *10*, 5845.
22. Chen, X. -L.; Shen, Y.; Gao, C.; Yang, J.; Sun, X.; Zhang, X.; Yang, Y.; Wei, G.; Xiang, J.; Sessler, J. L.; Gong, H. Regulating the Structures of Self-Assembled Mechanically Interlocked Moleculecular Constructs via Dianion Precursor Substituent Effects. *J. Am. Chem. Soc*. **2020**, *142*, 7443.
23. Ji, W.; Tang, Y.; Makam, P.; Jiao, Y. R.; Cai, K.; Wei, G.; Gazit, E. Expanding the Structural Diversity and Functional Scope of Diphenylalanine-Based Peptide Architectures by Hierarchical Coassembly. *J. Am. Chem. Soc*. **2021**, *143*, 17633.
24. Oh, B.; Yoon, E.; Gong, J.; Kim, J.; Driver, R. W.; Kim, Y.; Kim, W. Y.; Lee, H. Morphology Transformation of Foldamer Assemblies Triggered by Single Oxygen Atom on Critical Residue Switch. *Small* **2021**, *17*, 2102525.
25. Chen, Q.; Feng, Y.; Zhang, D.; Zhang, G.; Fan, Q.; Sun, S.; Zhu, D. Light-Triggered Self-Assembly of a Spiropyran-Functionalized Dendron into Nano-/Micrometer-Sized Particles and Photoresponsive Organogel with Switchable Fluorescence. *Adv. Funct. Mater*. **2010**, *20*, 36.
26. Jin, Q.; Zhang, L.; Liu, M. Solvent-Polarity-Tuned Morphology and Inversion of Supramolecular Chirality in a Self-Assembled Pyridylpyrazole-Linked Glutamide Derivative: Nanofibers, Nanotwists, Nanotubes, and Microtubes. *Chem. Eur. J*. **2013**, *19*, 9234.
27. Higashiguchi, K.; Taira, G.; Kitai, J.; Hirose, T.; Matsuda, K. Photoinduced Macroscopic Morphological Transformation of an Amphiphilic Diarylethene Assembly: Reversible Dynamic Motion. *J. Am. Chem. Soc*. **2015**, *7*, 2722.
28. Pang. X.; Yu. X.; Lan. H.; Ge. X.; Li. Y.; Zhen. X.; Yi. T. Visual Recognition of Aliphatic and Aromatic Amines Using a Fluorescent Gel: Application of a Sonication-Triggered Organogel. *ACS Appl. Mater. Interfaces* **2015**, *7*, 13569.
29. Grande. V.; Soberats. B.; Herbst. S.; Stepanenko. V.; Wurthner. F. Hydrogen-bonded perylene bisimide J-aggregate aqua material. *Chem. Sci*. **2018**, *9*, 6904.
30. Hou, I.; Diez-Cabanes, V.; Galanti, A.; Valašek, M.; Mayor, M.; Cornil, J.; Narita, A.; Samorì, P.; Müllen, K. Photomodulation of Two-Dimensional Self-Assembly of Azobenzene-Hexa-peri-hexabenzocoronene-Azobenzene Triads. *Chem. Mater*. **2019**, *31*, 6979.
31. Grzelczak, M.; Marza´n, L.; Klajn, R. Stimuli-Responsive Self-Assembly of Nanoparticles. *Chem. Soc. Rev*. **2019**, *48*, 1342.
32. Fu, H.; Yao, J. N. Size Effects on the Optical Properties of Organic Nanoparticles. *J. Am. Chem. Soc*. **200**1, *7*, 1434.
33. Patra, A.; Hebalkar, N.; Sreedhar, B.; Sarkar, M.; Samanta, A.; Radhakrishnan, T. P. Tuning the Size and Optical Properties in Molecular Nano/microcrystals: Manifestation of Hierarchical Interactions. *Small*, **2006**, *2*, 650.
34. Kim, D.; Kwon, J. E.; Park, S. Y. Fully Reversible Multistate Fluorescence Switching: Organogel System Consisting of Luminescent Cyanostilbene and Turn-On Diarylethene. *Adv. Funct. Mater*. **2018**, *28*, 1706213.
35. Wang, Q.; Li, Z.; Tao, D.; Zhang, Q.; Zhang, P.; Guo, D.; Jiang. Y. Supramolecular Aggregates as Sensory Ensembles. *Chem. Commun*. **2016**, *52*, 12929.
36. Miao, W.; Wang, S.; Liu, M. Reversible Quadruple Switching with Optical, Chiroptical, Helicity, and Macropattern in Self-Assembled Spiropyran Gels. *Adv. Funct. Mater*. **2017**, *27*, 1701368.
37. Kumar, V.; Sk, B.; Kundu, S.; Patra, A. Dynamic and Static Excimer: A Versatile Platform for Single Component White-Light Emission and Chelation-Enhanced Fluorescence. *J. Mater. Chem. C* **2018**, *6*, 12086.
38. Pallavi, P.; Kumar, V.; Hussain, M. D. W.; Patra, A. Excited-State Intramolecular Proton Transfer-Based Multifunctional Solid-State Emitter: A Fluorescent Platform with "Write-Erase-Write" Function. *ACS Appl. Mater. Interfaces* **2018**, *10*, 44696.
39. Cheng, H.; Li, Y.; Tang, B. Z.; Yoon, Y. Assembly Strategies of Organic-Based Imaging Agents for Fluorescence and Photoacoustic Bioimaging Applications. *Chem. Soc. Rev*. **2020**, *49*, 21.
40. Kundu, S.; Sk, B.; Pallavi, P.; Giri, A.; Patra, A. Molecular engineering approaches towards all-organic white light emitting materials. *Chem. Eur. J*. **2020**, *26*, 5557.
41. Rakshit, S.; Das, S.; Govindaraj, V.; Maini, R.; Kumar, A.; Datta, A. Morphological Evolution of Strongly Fluorescent Water Soluble AIEEgen-Triblock Copolymer Mixed Aggregates with Shape Dependent Cell Permeability. *J. Phys. Chem. B* **2020**, *124*, 10282.
42. Le, X.; Shang, H.; Wu, S.; Zhang, J.; Liu, M.; Zheng, Y.; Chen, T. Heterogeneous Fluorescent Organohydrogel Enables Dynamic Anti-Counterfeiting. *Adv. Funct. Mater*. **2021**, *31*, 2108365.

43. Das, S.; Kundu, S.; Sk, B.; Sarkar, M.; Patra, A. Thermally Activated Delayed Fluorescence in Dibenzopyridoquinoxaline-Based Nanoaggregates. *Org. Mater*. **2021**, *3*, 477.
44. Varghese, S.; Das, S. Role of Molecular Packing in Determining Solid-State Optical Properties of π-Conjugated Materials. *J. Phys. Chem. Lett*. **2011**, *2*, 863.
45. Sekiguchi, S.; Kondo, K.; Sei, Y.; Akita, M.; Yoshizawa, M. Engineering Stacks of V-Shaped Polyaromatic Compounds with Alkyl Chains for Enhanced Emission in the Solid State. *Angew. Chem. Int. Ed*. **2016**, *128*, 7020.
46. Sk, B.; Thakre, P.; Tomar, R. S.; Patra, A. A Pyridoindole-Based Multifunctional Bioprobe: pH-Induced Fluorescence Switching and Specific Targeting of Lipid Droplets. *Chem. Asian J*. **2017**, *18*, 2501.
47. Mendes, A. C.; Baran, E. T.; Reis, R. L.; Azevedo, H. S. Self-Assembly in Nature: Using the Principles of Nature to Create Complex Nanobiomaterials. WIREs *Nanomed. Nanobiotechnol*. **2013**, *5*, 582.
48. Po, C.; Tam, A. Y.; Yam, V. W. Tuning of Spectroscopic Properties Via Variation of the Alkyl Chain Length: A Systematic Study of Molecular Structural Changes on Self-Assembly of Amphiphilic Sulfonate-Pendant Platinum(II) bzimpy Complexes in Aqueous Medium. *Chem. Sci*. **2014**, *5*, 2688.
49. Zhang, L.; Wang, X.; Wang, T.; Liu, M. Tuning Soft Nanostructures in Self-assembled Supramolecular Gels: From Morphology Control to Morphology-Dependent Functions. *Small*, **2015**, *11*, 1025.
50. Rösch, A. T.; Reynaerts, R.; Lamers, B. A. G.; Mali, K. S.; Feyter, S. D.; Palmans, A. R. A.; Meijer, E. W. Double Lamellar Morphologies and Odd-Even Effects in Two- and Three-Dimensional *N*, *N*′-bis(n-alkyl)-naphthalenediimide Materials. *Chem. Mater*. **2021**, *33*, 8800.
51. Kang, M.; Gu, X.; Kwok, R. T. K.; Leung, C. W. T.; Lam, J. W. Y.; Li, F.; Tang, B. Z. A Near-Infrared AIEgen for Specific Imaging of Lipid Droplets. *Chem. Commun*. **2016**, *52*, 5957.
52. Olzmann, J. A.; Carvalho, P. Dynamics and Functions of Lipid Droplets. *Nat. Rev. Mol. Cell Biol*. **2019**, *20*, 137.
53. Cruz, A. L. S.; Barreto, E.; Fazolini, N. P. B.; Viola, J. P. B.; Bozza, P. T. Lipid Droplets: Platforms with Multiple Functions in Cancer Hallmarks. *Cell Death Dis*. **2020**, *11*, 105.
54. Collot, M.; Bou, S.; Fam, T. K.; Richert, L.; Mely, Y.; Danglot, L.; Klymchenko, A. S.; Probing Polarity and Heterogeneity of Lipid Droplets in Live Cells Using a Push-Pull Fluorophore. *Anal. Chem*. **2019**, *91*, 1928.
55. Yoshihara, T.; Maruyama, R.; Shiozaki, S.; Yamamoto, K.; Kato, S.; Nakamura, Y.; Tobita, S. Visualization of Lipid Droplets in Living Cells and Fatty Livers of Mice Based on the Fluorescence of π-Extended Coumarin Using Fluorescence Lifetime Imaging Microscopy. *Anal. Chem*. **2020**, *92*, 4996.
56. Wang, K. N.; Liu, L. Y.; Mao, D.; Xu, S.; Tan, C. P.; Cao, Q.; Mao, Z. W.; Liu, B. A Polarity-Sensitive Ratiometric Fluorescence Probe for Monitoring Changes in Lipid Droplets and Nucleus during Ferroptosis. *Angew. Chem. Int. Ed*. **2021**, *60*, 15095.
57. Collot, M.; Fam, T. K.; Ashokkumar, P.; Faklaris, O.; Galli, T.; Danglot, L.; Klymchenko, A. S. Ultrabright and Fluorogenic Probes for Multicolor Imaging and Tracking of Lipid Droplets in Cells and Tissues. *J. Am. Chem. Soc*. **2018**, *140*, 5401.
58. Zhao, Y.; Shi, W.; Li, X.; Ma, H. Recent Advances in Fluorescent Probes for Lipid Droplets. *Chem. Commun.* **2022**, doi.org/10.1039/D1CC05717K.
59. Lakowicz, J. R. Principles of Fluorescence Spectroscopy, Springer, New York, **2006**.
60. Berezin, M. Y.; Achilefu, S. Fluorescence Lifetime Measurements and Biological Imaging. *Chem. Rev*. **2010**, *110*, 2641.
61. Chen, X.; Jagadesan, P.; Valandro, S.; Hupp, J. T.; Schanze, K. S.; Goswami, S. Identifying the Polymorphs of Zr-Based Metal-Organic Frameworks via Time-Resolved Fluorescence Imaging. *ACS Materials Lett*. **2022**, *4*, 370.
62. Tian, M.; Wang, C.; Wang, L.; Luo, K.; Zhao, A.; Guo, C. C. Study on the Synthesis and Structure-Effect Relationship of Multi-Aryl Imidazoles with Their Fluorescence Properties. *Luminescence* **2014**, *29*, 540.
63. Tagare, J.; Vaidyanathan, S. Recent Development of Phenanthroimidazole-Based Fluorophores for Blue Organic Light-Emitting Diodes (OLEDs): An Overview. *J. Mater. Chem. C* **2018**, *6*, 10138.
64. Yang, L.; Wang, J.; Liu, B.; Han, G.; Wang, H.; Yang, L.; Zhao, J.; Han, M. Y.; Zhang, Z. Tracking Lipid Droplet Dynamics for the Discrimination of Cancer Cells by a Solvatochromic Fluorescent Probe. *Sens. Actuators B: Chem*. **2021**, *333*, 129541.
65. Walther, T. C.; Farese, R. V. The Life of Lipid Droplets. *Biochim. Biophys. Acta* **2009**, *1791*, 459.
66. Gao, M.; Su, H.; Li, S.; Lin, Y.; Ling, X.; Qin, A.; Tang, B. Z. An Easily Accessible Aggregation-Induced Emission Probe for Lipid Droplet-Specific Imaging and Movement Tracking. *Chem. Commun*. **2017**, *53*, 921.
67. Zheng, X.; Zhu, W.; Ni, F.; Ai, H.; Gong, S.; Zhou, X.; Sessler, J. L.; Yang, C. Simultaneous Dual-Colour Tracking Lipid Droplets and Lysosomes Dynamics Using a Fluorescent Probe. *Chem. Sci*. **2019**, *10*, 2342.
68. Zhang, X.; Yuan, L.; Jiang, J.; Hu, J.; Rietz, A.; Cao, H.; Zhang, R.; Tian, X.; Zhang, F.; Ma, Y.; Zhang, Z.; Uvdal, K.; Hu, Z. Light-Up Lipid Droplets Dynamic Behaviors Using a Red-Emitting Fluorogenic Probe. *Anal. Chem*. **2020**, *92*, 3613.